S373P Mutation of Spike Protein in SARS-CoV-2 Stabilizes Omicron

Bin Zheng[1], Yuelong Xiao[1], Bei Tong[2], Yutong Mao[1], Rui Ge[1], Fang Tian[1], Xianchi Dong[3,4], and Peng Zheng[1*]

1. State Key Laboratory of Coordination Chemistry, Chemistry and Biomedicine Innovation Center (ChemBIC), School of Chemistry and Chemical Engineering, Nanjing University, Nanjing, Jiangsu, 210023, China
2. Institute of Botany, Jiangsu Province and Chinese Academy of Sciences, Nanjing, 210014, China
3. State Key Laboratory of Pharmaceutical Biotechnology, School of Life Sciences, Nanjing University, Nanjing, 210023, China
4. Engineering Research Center of Protein and Peptide Medicine, Ministry of Education, China

*Correspondence: pengz@nju.edu.cn

Abstract: Recently, a cluster of several newly occurring mutations on Omicron, which is currently the dominant SARS-CoV-2 variant, are found at the (mechanically) stable β-core region of spike protein's receptor-binding domain (RBD), where mutation rarely happened before. Notably, the binding of SARS-CoV-2 to human receptor ACE2 via RBD happens in a dynamic airway environment, where mechanical force caused by coughing or sneezing occurs and applies to the proteins. Thus, we used atomic force microscopy-based single-molecule force spectroscopy (AFM-SMFS) to measure the stability of RBDs and found that the unfolding force of Omicron RBD increased by 20% compared with the wild-type. Molecular dynamics simulations revealed that Omicron RBD showed more hydrogen bonds in the β-core region due to the closing of the α-helical motif caused primarily by the S373P mutation, which was further confirmed by the experiment. This work reveals the stabilizing effect of the S373P mutation and suggests mechanical stability becomes another important factor in SARS-CoV-2 mutation selection.

The COVID-19 pandemic, caused by SARS-CoV-2, has been spreading worldwide for more than two years, primarily due to the continuous mutation of the virus[1,2]. As a single-stranded RNA virus that has infected a very large population, SARS-CoV-2 has undergone numerous mutations and rapidly adapts to the host. As the primary protein of the virus that binds to the angiotensin-converting enzyme 2 (ACE2) receptor of the host cell, the spike protein plays an essential role in the infectivity and transmissibility of the virus, showing a particularly high evolutionary rate (Fig. 1A)[3,4]. Mutations in the spike protein's receptor-binding domain (RBD) are the most dangerous because this domain is the direct contact point with ACE2. In addition, the majority of neutralizing antibodies target the RBD[5-7]. Indeed, all SARS-CoV-2 variants of concern (VOCs) that have been announced by the WHO possess several mutations in the RBD[8,9]. These mutations lead to higher transmission, and these VOCs completely replace the original strain. Thus, knowledge of the effect of each mutation on the RBD is of great importance for understanding and fighting the virus.

The very recent VOC, Omicron (B.1.1.529), has more than 30 mutations in the spike protein, 15 of which are in the RBD, and shows the highest transmission thus far (Fig. 1a)[10-12]. Among these mutations, many with known effects are present on the flexible receptor-binding motif (RBM; residues 438-506), which makes direct interactions with the ACE2 receptor [13]. For example, mutations such as E484A and Q493R evade antibody neutralization, and Q498R and N501Y enhance spike/ACE2 binding. However, although containing so many mutations, the binding affinity of the spike protein/RBD of Omicron to ACE2 does not increase significantly, only similar to previous VOC Alpha and Beta. Considering the much higher transmissibility, other mechanism/effect of new mutations in RBD for Omicron besides the enhancement of binding affinity or immunity escape is possible.

Interestingly, a cluster of several new mutations, G339D, S371L, S373P, and S375F (Fig. 1b-c), is located close to the β-core region in the Omicron RBD (OmicronRBD) [10]. The effects of these mutations on the virus are still largely unknown. RBD has two subdomains with different stabilities and functions. The first is the flexible RBM with a concave surface for direct binding with ACE2 where mutations modify its binding affinity happen most. The second is a structured five-stranded antiparallel β-sheet core region that is covered with two connecting α-helices on both sides (Fig. 1c, colored in red). This region serves as a stably folded scaffold for the RBM, and these newly occurring mutations (green) in Omicron with undetermined functions are found in this mechanically stable region. In fact, as the critical component of the virus, the stability of the spike protein plays an important role in its entry efficiency and viral transmission. Moreover, the binding of SARS-CoV-2 to the human host receptor ACE2 via the RBD happens in a dynamic airway environment, where mechanical force caused by coughing or sneezing occurs (Fig. 1c). Thus, viral attachment via RBD will be subject to the perturbations caused by mechanical force. Higher mechanical stability may support the binding of the virus to the human cell, especially under harsh conditions. Thus, we hypothesized that these new mutations modified the mechanical stability of Omicron and resulted in enhanced binding ability and transmission, and a new strategy to study its stability is needed.

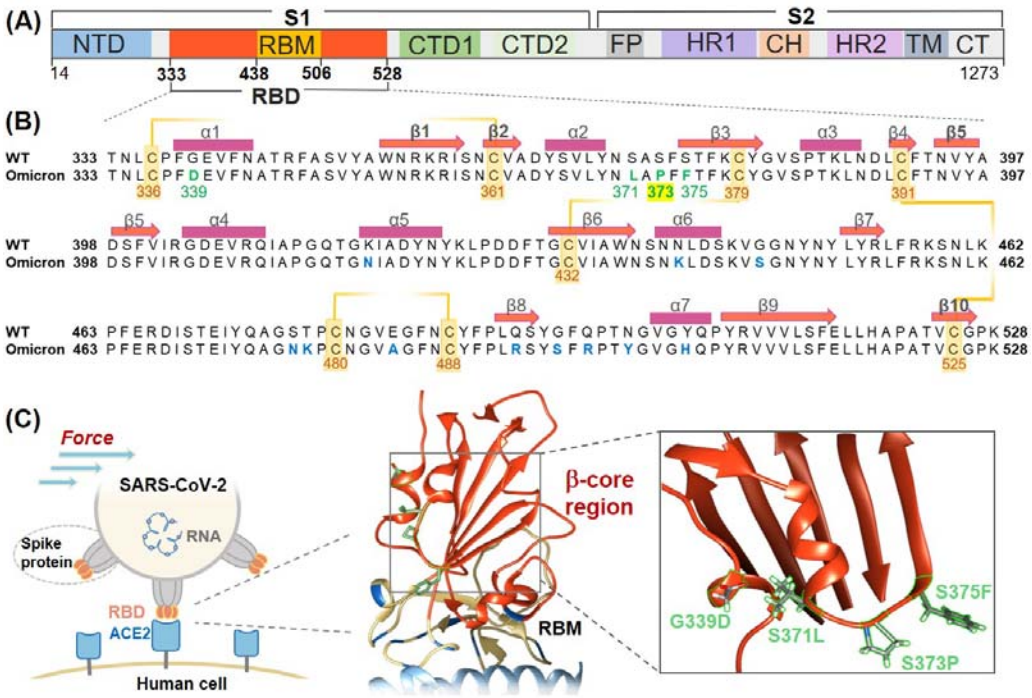

Fig. 1. Newly occurring mutations at the β-core region of RBD in spike protein subjected to mechanical force. a, Domain architecture of the full-length SARS-CoV-2 spike (S) protein. **b,** Sequence alignment of the Omicron variant (BA.1) with the wild-type RBD (333-528). The mutations are highlighted in green or blue. The orange line indicates the four disulfide bonds with the residue number shown. The secondary structure elements of the RBD (PDB code: 6ZGE) are marked with rectangles (helices) and arrows (strands) lines above the sequence. **c,** The spike protein trimers (gray) on the SARS-CoV-2 virus particles could bind to ACE2 (light blue) on the human cell surface via the RBDs (orange). **d,** Crystal structure of the RBD:ACE2 complex (PDB code: 7wbl). The RBD β-core region and RBM are colored orange and yellow, respectively. Part of ACE2 is represented in light blue. Details of the Omicron variant structure are illustrated in the right panel. Four mutations that first appeared in Omicron are colored green.

To this end, we used atomic force microscopy-based single-molecule force spectroscopy (AFM-SMFS) to investigate the mechanical stability of the RBDs from the wild-type (wtRBD) and Omicron variants. SMFS has been used to manipulate protein molecule(s) mechanically and studies the interaction between RBD/spike protein and its receptor in particular[14-16]. This technique mimics the external force from the dynamic airway on the protein during measurement, which the RBD may experience during binding to ACE2[17]. Previously, several groups have used SMFS to study the binding strength between the RBD and ACE2. They found that SARS-CoV-2 shows a higher binding force and binding energy to ACE2 than SARS-CoV-1[18,19]. We studied the effects of SARS-CoV-2 mutations and found that the N501Y mutation enhances RBD binding to ACE2, while K417N and E484K do not[20]. In addition to measuring protein-protein interaction, SMFS has been most widely used to measure the mechanical stability of the protein by (un)folding

experiments[21-27]. Here, we used it to measure RBDs and found a significant force increase of Omicron compared to WT. Moreover, computational simulations were used to gain mechanistic insight into the mechanical unfolding process, and the results revealed the key mutations for the observed stability increment and the underlying mechanism.

We used a high-precision AFM-SMFS system to measure the stability of the RBD[28,29]. For an accurate comparison, the target protein RBD is fused with other marker proteins with known stabilities that are site-specifically immobilized in the system. Asparaginyl endopeptidase (AEP)-mediated protein ligation was used for covalent RBD immobilization on a peptide-coated glass coverslip, in which enzymatic ligation occurred between their specific N-terminal NH_2-GL (Gly-Leu) dipeptide sequence and C-terminal NGL-COOH (Asp-Gly-Leu) tripeptide sequence (Fig. 2a, left panel)[30]. In addition, marker protein GB1 with a known unfolding force was used as an internal force caliper, and a dockerin-cohesin (Doc:Coh) noncovalent protein-protein interaction with a rupture force of ~500 pN was used as a single-molecule pulling handle [28,31]. Accordingly, the fused polyprotein Coh-$(GB1)_2$-RBD-GB1-NGL was designed and immobilized for precise AFM measurements (Fig. 2a).

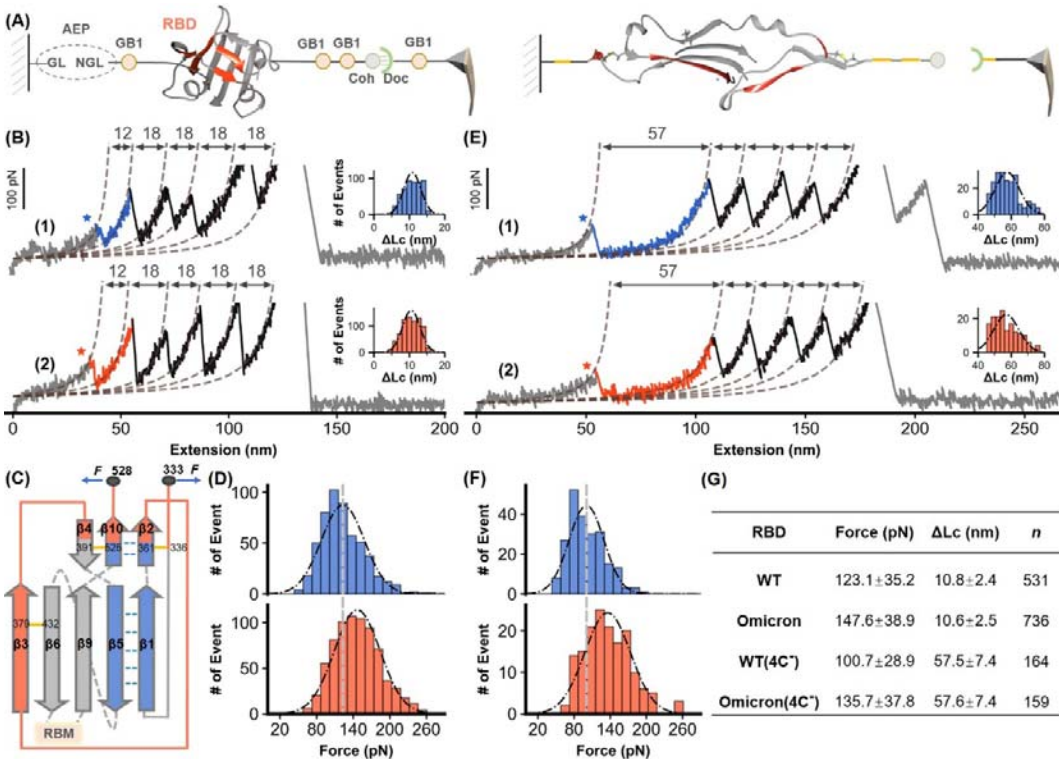

RBD	Force (pN)	ΔLc (nm)	n
WT	123.1±35.2	10.8±2.4	531
Omicron	147.6±38.9	10.6±2.5	736
WT(4C⁻)	100.7±28.9	57.5±7.4	164
Omicron(4C⁻)	135.7±37.8	57.6±7.4	159

Fig. 2. AFM unfolding experiment of wtRBD and OmicronRBD a, High-precision AFM-SMFS system to measure the mechanical stability of the RBD using the fused protein Coh-$(GB1)_2$-RBD-GB1-NGL. The protein was site-specifically immobilized to the glass surface using ligase AEP and could be picked up with a Doc-functionalized AFM tip via the Doc:Coh interaction (left panel). Then, the RBD and all other proteins were unfolded by stretching, and their mechanical stability was

measured accordingly (right panel). **b,** Representative curves showing a series of sawtooth-like peaks from the unfolding of the RBD with a ΔLc of ~11 nm and marker protein GB1 with a ΔLc of ~18 nm. The Omicron and WT variants are colored orange and blue, respectively. The histogram of ΔLc is shown in the inset. **c,** The unfolded fragments are depicted by their secondary structures. **d,** The unfolding force of the OmicronRBD is ~20% higher than that of the wtRBD. **e,** Unfolding of the RBD mutants with the deletion of two disulfide bonds (C391-C525, C379-C432) resulted in an elongated ΔLc from 12 nm to 57 nm, as expected. **f,** The force of the disulfide bonds-deleted Omicron RBD mutant was still higher than that of the WT. **g,** Detailed AFM data are shown.

Then, an AFM cantilever with a GB1-Doc-functionalized tip was used. By moving the tip toward the protein-immobilized surface, the RBD was picked up through the specific Doc:Coh interaction. Then, the tip retracted and all of the proteins/domains sequentially stretched and unfolded, ending with the rupture of the strongest Doc:Coh interaction. The mechanical stability of the RBD was measured accordingly (Fig. 2a, right). Finally, the tip moved to another spot on the surface and the cycle was repeated on different RBDs thousands of times. This system enables highly reliable and efficient AFM measurements and data analysis from a single molecule.

The fused protein containing wtRBD or OmicronRBD was built for AFM-SMFS measurements. Stretching led to a force-extension curve with sawtooth-like peaks from the unfolding of GB1 (18 nm) and a peak from the rupture of the Doc:Coh interaction (Figs. 2B and S1). In addition to these auxiliary signals, a force peak with a ΔLc of ~11 nm was observed for both constructs, which suggests that the signal must result from RBD unfolding. Statistically, the value was 10.8±2.4 nm for the wtRBD and 10.6±2.5 nm for the OmicronRBD. To confirm these results, we calculated the theoretical number of extendable residues upon RBD unfolding. First, there are four disulfide bonds present in the RBD, which cannot be broken, and the residues between them are locked[32]. Thus, RBD unfolding will lead to the extension of only 31 residues, from the first structured residue C361 to the last residue C391 (Fig. 2c, red). As a result, the theoretical ΔLc value is 10.3 nm (31*0.365 nm/aa-1.0 nm), agreeing well with the experimental value of ~11 nm and confirming that the peak was attributed to the RBD. Thus, the average unfolding force was 123.1 pN for wtRBD and 147.6 pN for OmicronRBD. These results support our hypothesis that the OmicronRBD has increased mechanical stability upon mutation.

To further verify that the observed data were from RBD unfolding, we deleted two disulfide bonds (C379-C432 and C391-C525) in the RBD by mutating the four cysteines to alanines. As a result, 190 residues that the two disulfide bonds had locked in the RBD and previously inextensible will be unfolded in this construct, which led to a larger ΔLc of 58.1 nm (162*0.365 nm/aa-1.0 nm)(Supplementary Fig. 2). Then, we performed the same AFM experiments on these two constructs. As expected, the 11 nm peak mostly disappeared, while a new peak with a ΔLc of ~58 nm was observed, confirming that the previous 11 nm peak was from the RBD. These values were 57.5 nm for the WT and 57.6 nm for the Omicron. Moreover, the unfolding force

of OmicronRBD (135.7 pN) was still higher than that of wtRBD (100.7 pN) for this mutant, again demonstrating the stronger stability of OmicronRBD than wtRBD.

To gain mechanistic insight into the considerable stability enhancement and pin down the exact mutation(s) responsible for this effect, we performed two different all-atom molecule dynamics simulations, focusing on the hydrogen bond in the β-core region of the RBD[33]. First, we performed steered molecular dynamics (SMD) simulations to visualize the mechanical unfolding process of the RBD and reveal the unfolding barrier/key force-bearing motif. Similar to the above experiment, the RBD was stretched with a constant pulling speed under a simulated force field and showed the force-extension trajectory (Fig. 3a, Video S1 for WT, Video S2 for Omicron). Indeed, the unfolding force of the OmicronRBD was generally higher than that of the wtRBD over the trajectory. This difference was quantitatively reflected by the potential of mean force analysis from irreversible pulling through Jarzynski's equality (Fig. S3), which gave a value of 205 kJ/mol vs. 184 kJ/mol (Fig. 3a, inset). Moreover, the SMD trajectory demonstrated that the major contributing factors to the unfolding barrier are from the peeling between β-strands 2 and 10 and β-strands 1 and 5, as shown by snapshots of the three key unfolding events (Fig. 3a, red). Therefore, the interaction between these β-strands determined the mechanical stability of the RBD.

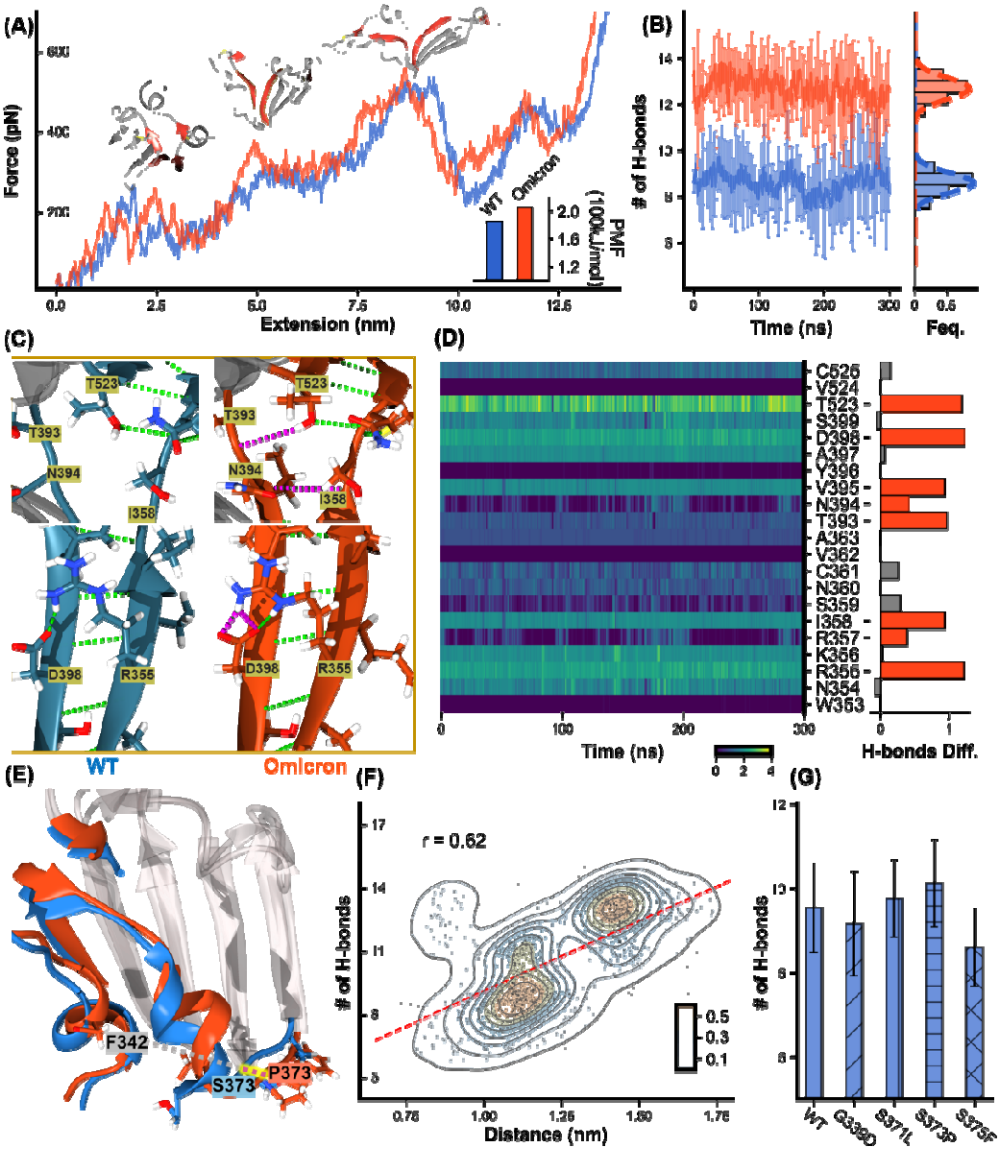

Figure 3. MD simulation results for wtRBD and OmicronRBD focusing on the four force-bearing β strands. (A) SMD force-extension trajectories of stretching wtRBD (blue) and OmicronRBD (orange). The three key snapshots show the renderings of the RBDs at different times. The four force-bearing β-strands, β2/β10 and β1/β5, in the β-sheet are colored red. Inset: the potential of mean force (PMF) calculated. **(B)** MD simulations show the number of hydrogen bonds formed in the four β-strands. **(C)** The enlarged structure shows the hydrogen bonds (dashed line) in the four β-strands. Additional H-bonds in Omicron are colored in pink. **(D)** The evolution of the number of hydrogen bonds for each residue involved in β2/β10 and β1/β5 during the MD simulations. The difference in hydrogen bonds between Omicron and WT was shown in the right panel, and the red bars indicate a noticeable increment in Omicron compared to WT. **(E)** Overlapped structure of Omicron and WT focusing on the β-core region of the RBD shows that the conformation of α2 in Omicron has changed. The distance between P373 and F342 in Omicron is longer (red

dash line) than that between S373 and F342 in the WT. **(F)** The relationship between the distances of residues 373 near α2 and F342 near α1 (as a reference point) and the number of hydrogen bonds was extracted from multiple MD simulations. **(G)** By introducing a single mutation into the wtRBD, MD simulations show that S371L and S373P increase the number of hydrogen bonds in the region.

Thus, we performed MD simulations to determine the number of hydrogen bonds in these four β-strands of the wtRBD (Video S3) and OmicronRBD (Video S4). After 300 *ns* of simulation, ~9 hydrogen bonds were present in the wtRBD, while ~13 bonds were found in the OmicronRBD, on average (Fig. 3b). Moreover, a detailed analysis of the hydrogen bond number for each residue along the simulation for both wtRBD and OmicronRBD was also performed, showing that several residues participated in more hydrogen bonds in the Omicron (Figs. 3c, 3d, and S4).

To rationalize the origin of this difference in the number of hydrogen bonds, we overlapped the structures of the WT and Omicron RBDs, focusing on the β-core region. Notably, α-helix 2 in Omicron moved toward the β-sheet core, as reflected in the cryo-electron microscopy (cryo-EM) structure (Supplementary Fig. 5). Although this movement is not apparent in cryo-EM structure with a fixed conformation, it can be readily inspected through the structure from MD simulations with multiple dynamic conformations (Fig. 3e, highlighted and in red). To validate the relationship between this structural change and the number of hydrogen bonds, we performed ten times of MD simulations (300 *ns*) and chose every six ns to calculate the number of hydrogen bonds in each simulation. Since the position of α-helix 1 is relatively consistent, we chose it as a reference point, and measured the distance between residue 373 in α-helix 2 and residue F342 in α-helix 1 at each section. These distances were plotted along with the number of hydrogen bonds. As shown in Fig. 3f, the longer the distance between them, the more hydrogen bonds are generally observed. The relationship between distance of residue 371/375 to residue F432 and the number of hydrogen bonds is not very significant (Supplementary Fig. 6).

The new mutations G339D, S371L, S373P, and S375P in the core region of the RBD are close to α-helix 2, suggesting their roles in this structural change. Thus, we built a single mutation into the wtRBD for MD simulations (n=10) and analyzed the corresponding number of hydrogen bonds. On average, wtRBD(S373P) showed the highest increase of two hydrogen bonds, and wtRBD(S371L) showed the modest addition of one hydrogen bond, and the effects for the other two mutations were trivial (Fig. 3g). Thus, it appears that the S373P mutation rigidifies the local polypeptide chain, leading to the inward movement of helix 2 from the structure. Consequently, MD simulations revealed that S371L and S373P most likely account for the increased stability of the OmicronRBD.

Inspired by the simulation results, we built four wtRBD mutants in the polyprotein constructs, focusing on residues 371 and 373 for experimental confirmation. First, wtRBD(S371L) and wtRBD(S373P) were constructed, in which these two mutations found in Omicron were added to the wtRBD. As expected, the unfolding signal of the RBD was the same except for the force (Fig. 4a and S7). The AFM results for wtRBD(S371L) showed no force increment (123.4 pN), while

wtRBD(S373P) showed a considerable increment of 20 pN (143.8 pN).

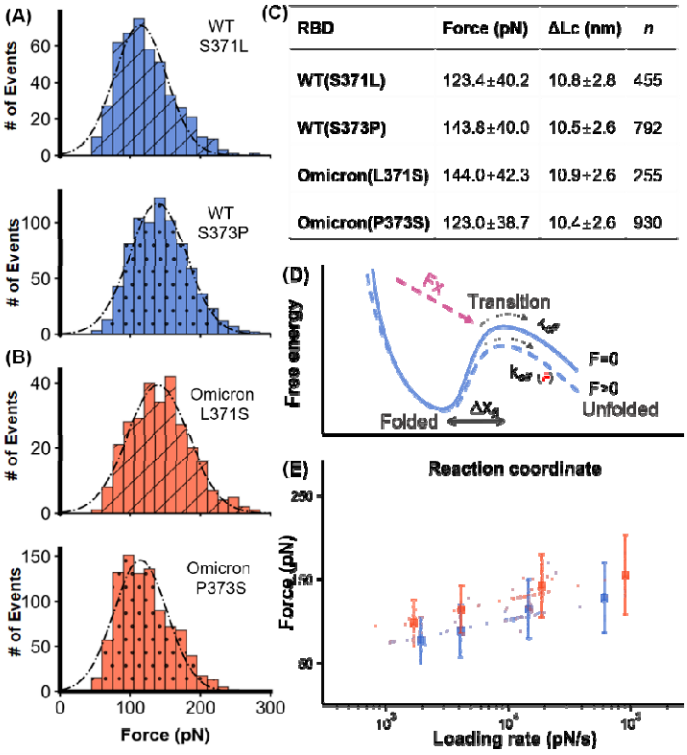

RBD	Force (pN)	ΔLc (nm)	n
WT(S371L)	123.4±40.2	10.8±2.8	455
WT(S373P)	143.8±40.0	10.5±2.6	792
Omicron(L371S)	144.0±42.3	10.9±2.6	255
Omicron(P373S)	123.0±38.7	10.4±2.6	930

Figure 4. AFM-SMFS results of RBDs with a point mutation a-b, Unfolding force histograms of wtRBD(S371L), wtRBD(S373P), OmicronRBD(L371S), and OmicronRBD(P373S) showing that residue 373 is the primary site for the fine-tuning of RBD stability with the biggest force change upon mutation. **c,** The unfolding force of RBDs is shown. **d,** The free-energy potential between folded state and transition state of the protein in the absence (solid, blue) and the presence of an externally applied pulling force (dashed, blue). **e,** The unfolding forces of the WT and Omicron RBDs show a linear relationship with the logarithm of the loading rate.

Moreover, we built OmicronRBD(L371S) and OmicronRBD(P373S), in which the mutation found in Omicron is reverted back to the residues present in the wtRBD while keeping all other mutations. The unfolding force decreased in these RBDs. The unfolding force of OmicronRBD(L371S) decreased slightly to 144.0 pN, while that of OmicronRBD(P373S) decreased to 123.0 pN (Fig. 4b-c). Also, we built a similar point mutation on the remaining two residues, 339 and 375, in the cluster and performed the same AFM experiments. Agreeing with the computational simulation, the mutation on these two sites did not change the mechanical stability of the RBD (Supplementary Fig. S8). Consequently, this experimental measurement showed that the enhanced stability of OmicronRBD can be mainly attributed to the S373P mutation.

Finally, the unfolding kinetics of the wtRBD and OmicronRBD were determined by stretching the proteins at different velocities during a force loading rate experiment[34-36]. In force spectroscopy measurements, the application of external

mechanical force lowers the activation energy of protein unfolding (Fig. 4d). Thus, the unfolding force is proportional to the logarithm of the loading rate, which describes the effect of the force applied on the protein over time. As expected, the plots showed a linear relationship (Fig. 4e and Supplementary Fig. 9). From the fit, we estimated the unfolding rate (k_{off}) value and the length scale of the energy barrier (Δx) value. The k_{off} was 0.59±0.43 s^{-1} (value and fitting error) for the wtRBD and 0.12±0.12 s^{-1} for the OmicronRBD. The k_{off} of WT(S373P) decreased to the similar value as that of OmicronRBD, while WT(S371L) remained mostly unchanged. The kinetic results also showed a stabilized OmicronRBD with a lower off rate than the wtRBD and the mutation S373P plays an import role in the increment of mechanical stability.

Coronaviruses are large, single-stranded RNA viruses evolving with a remarkable mutation rate, as evidenced by the transmission of several VOCs of SARS-CoV-2 in only the past two years. In addition to neutral mutations, the effect of many accumulated mutations has been revealed. In this study, we combined experimental and computational approaches to study the mechanical stability of the OmicronRBD and determine the effect of mutation S373P in the β-core region. First, the AFM measurements showed an unfolding force for that OmicronRBD that was 20% higher than its characteristic unfolding. To the best of our knowledge, this is the first experimental work to quantitatively show higher mechanical stability of the OmicronRBD. Then, MD simulations uncovered its detailed unfolding pathway and revealed the underlying mechanism of the stability increment, which is due to the increased number of hydrogen bonds caused by the mutations S373P and S371L.

From a structural perspective, two subdomains with different mechanical stability are present in the RBD. The RBM dominates ACE2 binding and receptor specificity. Before Omicron, most accumulating mutations in the RBD occurred in the RBM. In addition, mutations in the other subdomain, the β-core region consisting of a central β-sheet flanked by α-helices, were rare. In fact, there are four disulfide bonds in the RBD, strongly supporting the overall structure of the RBD and its function. To date, no naturally occurring variant with mutations to these cysteine residues has been observed. Intended cysteine mutation results in the dysfunction of the RBD binding to ACE2, highlighting the importance of a stable RBD structure supported by the disulfide bonds. In this work, we found that a mutation in the β-core domain can fine-tune the stability of the RBD and is thus highly likely to contribute to RBD function and virus transmission.

This stabilizing effect can also be explained by the dynamic environment the RBD experiences during receptor binding. The binding of SARS-CoV-2 to the human host receptor ACE2 via the RBD occurs in a dynamic airway environment where mechanical force caused by coughing or sneezing occurs. Thus, viral attachment and the RBD, in particular, will be subjected to the perturbation of mechanical force, and RBD stability can be related to virus transmission. Indeed, as the critical component of the virus, the stability of the spike protein plays an essential role in its entry efficiency and viral transmission [37].

In addition to discovering the effect of mutation S373P for SARS-CoV-2, this

work revealed a new way that nature used to increase protein's mechanical stability by using proline mutation. Proline mutation is often used to decrease protein's stability by disrupting the hydrogen bond networks in β-sheet region of the protein. Here, by introducing proline in the loop close to the β-sheet region, more hydrogen bonds are formed and stabilize the region. Thus, a new strategy to design proteins with enhanced stability is demonstrated, and the continuing mutation/evolution leading to the increase of SARS-CoV-2 protein stability can be recognized.

Consequently, we proposed that an evolution to promote higher mechanical stability may occur during (SARS-CoV-2) virus mutation, especially in the spike protein. As discussed, mechanical forces applied to the spike protein are unavoidable during receptor binding. Therefore, a more mechanically stable spike protein and RBD may lead to an improved binding ability to ACE2 or survival time, especially in harsh environments with higher mechanical perturbation. The importance of mechanical forces in immunity has been demonstrated, such as tuning T-cell receptor sensitivity to mechanical forces for better CAR T-cell therapy[38]. And so many single-molecule studies of protein, DNA, and RNA show the relationship between the effect of mechanical force and their folding and function[39-44]. Thus, mechanical stability can become another factor in SARS-CoV-2 mutation selection.

In addition to the experimental results, the computational data provide essential mechanistic insight into the OmicronRBD, and these simulations were essential parts of our work[45,46]. First, SMD simulations revealed the key unfolding barrier of the RBD and guided us to focus on β-strands 2/10 and β-strands 1/5 and their hydrogen bonds. Moreover, the computational results demonstrate the relationship between the number of hydrogen bonds and the inward shift of helix 2, thus implying the role of the nearby mutations in RBD stability. Finally, two mutations, S371L and S373P, were identified as being responsible for the enhanced stability of the OmicronRBD. Based on the computational results, the experimental measurements showed that S373P is the mutation primarily responsible for enhanced protein stability.

During the submission of this work, Omicron's sister strains, BA.2 (B.1.1.529.2), BA.3 (B.1.1.529.3), BA.4 (B.1.1.529.4) and BA.5 (B.1.1.529.5) were identified and were shown to have higher transmissibility[47-50]. Interestingly, the mutations found in the β-core region of BA.1 remain in the other four Omicron strains. Mutation S373P is identical and relatively conservative, while S371 is mutated to the more hydrophobic residue leucine in BA.1 and phenylalanine in BA.2-5 further demonstrating the importance of this mutation and suggesting its effect on higher transmission. Since we cannot predict future mutations and emerging variants of SARS-CoV-2, it is critical to maintain surveillance of existing variants and mutations and study their effects.

METHODS SUMMARY

References and Notes:

1 Li, F. Structure, Function, and Evolution of Coronavirus Spike Proteins. *Annu. Rev. Virol.* **3**, 237-261 (2016).

2 Wu, F. *et al.* A new coronavirus associated with human respiratory disease in China. *Nature* **579**, 265-269 (2020).
3 Lan, J. *et al.* Structure of the SARS-CoV-2 spike receptor-binding domain bound to the ACE2 receptor. *Nature* **581**, 215-220 (2020).
4 Thomas G. Ksiazek, Goldsmith, C. S. & Zaki, S. R. A novel coronavirus associated with severe acute respiratory syndrome. *N. Engl. J. Med.* **348**, 1953-1966 (2003).
5 Starr, T. N. *et al.* Deep Mutational Scanning of SARS-CoV-2 Receptor Binding Domain Reveals Constraints on Folding and ACE2 Binding. *Cell* **182**, 1295-1310 e1220 (2020).
6 Jackson, C. B., Farzan, M., Chen, B. & Choe, H. Mechanisms of SARS-CoV-2 entry into cells. *Nat. Rev. Mol. Cell Biol.* **23**, 3-20 (2022).
7 Han, Y. *et al.* Covalently Engineered Protein Minibinders with Enhanced Neutralization Efficacy against Escaping SARS-CoV-2 Variants. *J. Am. Chem. Soc.* **144**, 5702-5707 (2022).
8 Harvey, W. T. *et al.* SARS-CoV-2 variants, spike mutations and immune escape. *Nat. Rev. Microbiol.* **19**, 409-424 (2021).
9 Weisblum, Y. *et al.* Escape from neutralizing antibodies by SARS-CoV-2 spike protein variants. *Elife* **9**, e61312 (2020).
10 Yin, W. *et al.* Structures of the Omicron spike trimer with ACE2 and an anti-Omicron antibody. *Science* **375**, 1048-1053 (2022).
11 Elliott, P. *et al.* Rapid increase in Omicron infections in England during December 2021: REACT-1 study. *Science* **375**, 1406-1411 (2022).
12 Cui, Z. *et al.* Structural and functional characterizations of infectivity and immune evasion of SARS-CoV-2 Omicron. *Cell* **185**, 860-871 e813 (2022).
13 Zhang, J. *et al.* Structural and functional impact by SARS-CoV-2 Omicron spike mutations. *Cell Rep.* **39**, 110729 (2022).
14 Alsteens, D. *et al.* Nanomechanical mapping of first binding steps of a virus to animal cells. *Nat. Nanotechnol.* **12**, 177-183 (2017).
15 Cuellar-Camacho, J. L. *et al.* Quantification of Multivalent Interactions between Sialic Acid and Influenza A Virus Spike Proteins by Single-Molecule Force Spectroscopy. *J. Am. Chem. Soc.* **142**, 12181-12192 (2020).
16 Dufrene, Y. F. *et al.* Five challenges to bringing single-molecule force spectroscopy into living cells. *Nat. Methods* **8**, 123-127 (2011).
17 Bauer, M. S. *et al.* A tethered ligand assay to probe SARS-CoV-2:ACE2 interactions. *Proc. Natl. Acad. Sci. U. S. A.* **119**, e2114397119 (2022).
18 Cao, W. *et al.* Biomechanical characterization of SARS-CoV-2 spike RBD and human ACE2 protein-protein interaction. *Biophys. J.* **120**, 1011-1019 (2021).
19 Yang, J. *et al.* Molecular interaction and inhibition of SARS-CoV-2 binding to the ACE2 receptor. *Nat. Commun.* **11**, 4541 (2020).
20 Tian, F. *et al.* N501Y mutation of spike protein in SARS-CoV-2 strengthens its binding to receptor ACE2. *Elife* **10**, e69091 (2021).
21 Rief, M., Gautel, M., Oesterhelt, F., Fernandez, J. M. & Gaub, H. E.

Reversible unfolding of individual titin immunoglobulin domains by AFM. *Science* **276**, 1109-1112 (1997).

22 Yu, H., Siewny, M. G., Edwards, D. T., Sanders, A. W. & Perkins, T. T. Hidden dynamics in the unfolding of individual bacteriorhodopsin proteins. *Science* **355**, 945-950 (2017).

23 Cao, Y. & Li, H. B. Engineered elastomeric proteins with dual elasticity can be controlled by a molecular regulator. *Nat. Nanotechnol.* **3**, 512-516 (2008).

24 Zhuang, X. & Rief, M. Single-molecule folding. *Curr. Opin. Struct. Biol.* **13**, 88-97 (2003).

25 Alonso-Caballero, A. *et al.* Protein folding modulates the chemical reactivity of a Gram-positive adhesin. *Nat. Chem.* **13**, 172-181 (2021).

26 Scholl, Z. N., Yang, W. T. & Marszalek, P. E. Direct Observation of Multimer Stabilization in the Mechanical Unfolding Pathway of a Protein Undergoing Oligomerization. *Acs Nano* **9**, 1189-1197 (2015).

27 Perales-Calvo, J., Giganti, D., Stirnemann, G. & Garcia-Manyes, S. The force-dependent mechanism of DnaK-mediated mechanical folding. *Sci. Adv.* **4**, eaaq0243 (2018).

28 Stahl, S. W. *et al.* Single-molecule dissection of the high-affinity cohesin-dockerin complex. *Proc. Natl. Acad. Sci. U. S. A.* **109**, 20431-20436 (2012).

29 LeBlanc, M. A., Fink, M. R., Perkins, T. T. & Sousa, M. C. Type III secretion system effector proteins are mechanically labile. *Proc. Natl. Acad. Sci. U. S. A.* **118**, e2019566118 (2021).

30 Deng, Y. *et al.* Enzymatic biosynthesis and immobilization of polyprotein verified at the single-molecule level. *Nat. Commun.* **10**, 2775 (2019).

31 Cao, Y., Lam, C., Wang, M. & Li, H. Nonmechanical protein can have significant mechanical stability. *Angew. Chem. Int. Ed.* **45**, 642-645 (2006).

32 Alegre-Cebollada, J. *et al.* S-Glutathionylation of Cryptic Cysteines Enhances Titin Elasticity by Blocking Protein Folding. *Cell* **156**, 1235-1246 (2014).

33 Bernardi, R. C. *et al.* Mechanisms of Nanonewton Mechanostability in a Protein Complex Revealed by Molecular Dynamics Simulations and Single-Molecule Force Spectroscopy. *J. Am. Chem. Soc.* **141**, 14752-14763 (2019).

34 Merkel, R., Nassoy, P., Leung, A., Ritchie, K. & Evans, E. Energy landscapes of receptor-ligand bonds explored with dynamic force spectroscopy. *Nature* **397**, 50-53 (1999).

35 Dudko, O. K., Hummer, G. & Szabo, A. Theory, analysis, and interpretation of single-molecule force spectroscopy experiments. *Proc. Natl. Acad. Sci. U. S. A.* **105**, 15755-15760 (2008).

36 Bustamante, C., Chemla, Y. R., Forde, N. R. & Izhaky, D. Mechanical processes in biochemistry. *Annu. Rev. Biochem.* **73**, 705-748 (2004).

37 Zhang, Q. *et al.* Molecular mechanism of interaction between SARS-CoV-2 and host cells and interventional therapy. *Signal Transduct. Target Ther.* **6**, 233 (2021).

38 Zhao, X. *et al.* Tuning T cell receptor sensitivity through catch bond engineering. *Science* **376**, eabl5282 (2022).
39 Chen, Y., Radford, S. E. & Brockwell, D. J. Force-induced remodelling of proteins and their complexes. *Curr. Opin. Struct. Biol.* **30**, 89-99 (2015).
40 Gruszka, D. T. *et al.* Cooperative folding of intrinsically disordered domains drives assembly of a strong elongated protein. *Nat. Commun.* **6**, 7271 (2015).
41 Zhao, M. & Woodside, M. T. Mechanical strength of RNA knot in Zika virus protects against cellular defenses. *Nat. Chem. Biol.* **17**, 975-981 (2021).
42 Dong, X. *et al.* Force interacts with macromolecular structure in activation of TGF-beta. *Nature* **542**, 55-59 (2017).
43 Mohapatra, S., Lin, C.-T., Feng, X. A., Basu, A. & Ha, T. Single-Molecule Analysis and Engineering of DNA Motors. *Chem. Rev.* **120**, 36-78 (2020).
44 Le, S., Yu, M. & Yan, J. Direct single-molecule quantification reveals unexpectedly high mechanical stability of vinculin-talin/alpha-catenin linkages. *Sci. Adv.* **5**, eaav2720 (2019).
45 Zhou, W. *et al.* Large-scale state-dependent membrane remodeling by a transporter protein. *Elife* **8**, e50576 (2019).
46 Pavlova, A. *et al.* Machine Learning Reveals the Critical Interactions for SARS-CoV-2 Spike Protein Binding to ACE2. *J. Phys. Chem. Lett.* **12**, 5494-5502 (2021).
47 Yamasoba, D. *et al.* Virological characteristics of the SARS-CoV-2 Omicron BA.2 spike. *Cell* (2022).
48 Arora, P. *et al.* Comparable neutralisation evasion of SARS-CoV-2 omicron subvariants BA.1, BA.2, and BA.3. *Lancet Infect. Dis.* (2022).
49 Gangavarapu, K. *et al.* Outbreak. info genomic reports: scalable and dynamic surveillance of SARS-CoV-2 variants and mutations. *medRxiv* (2022).
50 Kimura, I. *et al.* Virological characteristics of the novel SARS-CoV-2 Omicron variants including BA. 2.12. 1, BA. 4 and BA. 5. *bioRxiv* (2022).

Acknowledgments: The numerical calculations in this paper have been done on the computing facilities in the High-Performance Computing Center (HPCC) of Nanjing University.The authors thank inspiring discussions with Prof. Thomas T. Perkins and Prof. Michael M. Nash.

Funding:
National Natural Science Foundation of China grant No. 21977047 (PZ)
Fundamental Research Funds for the Central Universities 14380205 (PZ)
Natural Science Foundation of Jiangsu Province No. BK20200058, BK20202004 (PZ)

Author contributions:
Conceptualization & Methodology: PZ
Investigation: BZ, YRX, BT, RG, XCD
Visualization: PZ, BZ
Funding acquisition: PZ, XCD
Project administration & Supervision: PZ

Writing – original draft: PZ, BZ

Competing interests: The authors declare no competing interests.

Data and materials availability: All data are available in the main text or the supplementary materials

Supplementary Materials

Materials and Methods

Supplementary Text

Figs. S1 to S9

References (*47–57*)

Movies S1 to S4

SUPPLEMENTARY MATERIALS

Materials and Methods

Protein expression and purification. The genes were ordered from Genscript Inc. The wtRBD and OmicronRBD constructs contain the SAS-CoV-2 spike protein (residues 319-591), followed by a GGGGS linker and an 8XHis tag in pcDNA3.4 modified vector. They were expressed in Expi293 cells with OPM-293 CD05 serum-free medium (OPM Biosciences)(*20*). In addition to these two RBDs, most RBDs (residues 333-528) were constructed as a fused polyprotein Coh-$(GB1)_2$-RBD-GB1-NGL for high-precision AFM measurement and thus expressed in *E. coli* BL21(DE3) using pQE80L vector. The *BamH*I-*Bgl*II-*Kpn*I three-restriction enzyme system was used for the stepwise construction of the genes for polyproteins. For protein purification of RBD with His-tag, culture supernatant was passed through a Ni-NTA affinity column (Qiagen). Proteins were further purified by gel filtration (Superdex^{TM} 200 Increase 10/30GL, GE Healthcare).

*Oa*AEP1(C247A) is cysteine 247 to alanine mutant of asparaginyl endoproteases 1 from *oldenlandia affinis*, abbreviated as AEP here (*30*, *47*). ELP is the elastin-like polypeptides (*48*). Their expression and purification protocols can be found in references. RBD mutants, including wtRBD(S371L), wtRBD(S373P), OmicronRBD (L371S), and OmicronRBD (P373S), were generated using the QuikChange kit. Their sequences were all verified by direct DNA sequencing.

AFM-SMFS experiment. The AFM cantilever/tip made of silicon nitride (MLCT-BIO-DC, Bruker Corp.) was used. The detailed protocol for AFM tip functionalization and protein immobilization on the glass coverslip can be found in references (*30*, *49*). In short, the tip and glass coverslip were coated with the amino group by amino-silanization. Then, the maleimide group for cysteine coupling was added on the amino-functionalized surface using the hetero-bifunctional crosslinker sulfosuccinimidyl 4-(N-maleimidomehthyl) cyclohexane-1-carboxylate) (Sulfo-SMCC, Thermo Scientific). Next, the peptide GL-ELP_{20}-C or C-ELP_{20}-NGL was reacted to the maleimide via the cysteine, respectively. The long ELP_{20} serves as a spacer to avoid non-specific interaction between the tip and the surface as well as a signature for the single-molecule event. Finally, target protein RBDs with C-terminal NGL sequence or GB1-Doc with N-terminal GL sequence can be site-specifically linked to the coverslip or tip by ligase AEP, respectively.

Atomic force microscope (Nanowizard4, JPK) was used to acquire the force-extension curve. The D tip of the MLCT-Bio-DC cantilever was used. Its accurate spring constant was determined by a thermally-induced fluctuation method (*50*). Typically, the tip contacted the protein-immobilized surface for 400 *ms* under an indentation force of 450 pN to ensure a site-specifically interaction. Then, moving the tip up vertically at a constant velocity (1 μm/s, if not specified), the polyprotein unfolded. Then, the tip moved to another place to repeat this cycle several thousands of times. As a result, a force-extension curve was obtained, which was analyzed using JPK data process analysis software.

Bell-Evans model to extract kinetics. The RBD-ACE2 complex dissociation in the AFM experiment is a non-equilibrium process that can be modeled as an all-or-none two-state process with force-dependent rate constant k(F). The rate constant can be described by Bell-Evans' model (*34*):

$$k(F) = k_{\text{off}}\exp\left(\frac{F\Delta x}{k_b T}\right) \quad (1)$$

$k(F)$ is the protein unfolding rate under a particular force F, k_{off} is the unfolding rate constant under zero force, Δx is the distance between the unfolded state and the transition state. For the dynamic force spectroscopy measurements, the slope a of the force−extension curves immediately before the unfolding event (~2 nm) was first determined to obtain the average loading rate ($r = av$, where v is the velocity). The Bell-Evans model was used to fit all the data (1), yielding the spontaneous unfolding rate, and the distance from the folded state to the transition state with the following equation:

$$F = \frac{k_b \mathrm{T}}{\Delta x}\ln\left(\frac{\Delta x}{k_{\text{off}} k_b \mathrm{T}}\right) + \frac{k_b \mathrm{T}}{\Delta x}\ln(\mathrm{r}) \quad (2)$$

Four different pulling velocities, 0.2 µm/s, 0.4 µm/s, 1 µm/s, and 4 µm/s were used. The relationship between the most probable unfolding force and loading rate was obtained on a log scale, which is fitted by a linear line as equation (2).

MD simulation for RBD unfolding. To reveal the unfolding pathway of RBD under mechanical load, we performed steered molecular dynamics (SMD) simulations using NAMD(*51, 52*). Simulation systems were prepared using CHARMM-GUI (*53*). The structures of the RBDs were prepared following established protocols. For the WT, the structure had been solved by Electron Microscopy at 2.60 Å resolution and is available at the protein data bank (PDB ID: 6zge). The Omicron had also been solved by Electron Microscopy, at 3.5 Å resolution, and is available at the protein data bank (PDB ID: 7tl1). After extracting residues 333 to 528 in part A both of them, the RBDs were solvated and the net charge of the proteins were neutralized using a 150 mM salt concentration of sodium chloride. Disulfide bonds and the glycans at N343 were included following the literature information. SMD simulations were performed employing the NAMD molecular dynamics package. The CHARMM36 force field along with the TIP3 water model was used to describe all systems. The simulations were performed assuming periodic boundary conditions in the NpT ensemble with temperature maintained at 298 K using Langevin dynamics for pressure, kept at 1 bar, and temperature coupling (*54*). Before the MD simulations, all the systems were submitted to an energy minimization protocol for 5,000 steps. MD simulations with position restraints in the protein backbone atoms were performed for 1.0 *ns* and served to pre-equilibrate systems before the 10 *ns* equilibrium MD runs. To characterize the unfolding pathway of RBDs, ten times of SMD simulations with constant stretching velocity employed a pulling speed of 5.0 Å/ns and a harmonic constraint force of 7.0 kcal/mol/Å was applied for 30.0 ns. In this step, SMD were employed by harmonically

restraining the position of the C-terminus and pulling on the N-terminus of the RBDs (WT or Omicron). Each system was run 10 times. Simulation force-extension traces were analyzed analogously to experimental data. Data were analyzed by python-based Jupyter notebooks. Jarzynski's equality is applied to potential mean force (PMF) from SMD simulations (*55*). We also performed 60 times of SMD simulations with a pulling speed of 20 Å/ns to calculate the PMF.

MD simulations were performed utilizing the GROMACS 2021 package. And all simulation systems, including the mutation (G339D, S371L, S373P, or S375F), is established with similar procedures. All the input files were generated from CHARMM-GUI. The system's environment changed at 298 K (NVT ensemble) and subsequently at 298 K and 1 bar (NPT ensemble). We performed 300 ns MD simulations 10 times. And the number of hydrogen bonds formed between β2/β10 and β1/β5 (residue 353 to 363, 394 to 400, 523 to 526) was analyzed by the plug-in program *hbond* in GROMACS(*56*). The cutoff parameters of the hydrogen bond analysis program were defaulted values (3.5 Å and 30°). It means that when the distance between donor D and acceptor A was shorter than 3.5 Å, as well as the bond angle H–D is smaller than 30.0°, it is regarded as a hydrogen bond. Hydrogen bond formation for every residue between β2/β10 and β1/β5 is also generated by the same plug-in program, executed by a Python script. The distance between the Cα atoms of the 373 and 343 residues during the MD simulations of WT and Omicron was calculated by another plug-in program *distance* and organized by a python script to form a scatter plot with the number of hydrogen bonds. Then we use the pearsonr function in the scipy module to evaluate the correlation between the number of hydrogen bonds and the distance between residue 371 and 343 (*57*).

Supplementary Text

Protein sequences:

His6-Coh-GB1-GB1-RBD**(XX)**-GB1-NGL
MRGSHHHHHHGSMGTALTDRGMTYDLDPKDGSSAATKPVLEVTKKVFDTAA
DAAGQTVTVEFKVSGAEGKYATTGYHIYWDERLEVVATKTGAYAKKGAALE
DSSLAKAENNGNGVFVASGADDDFGADGVMWTVELKVPADAKAGDVYPID
VAYQWDPSKGDLFTDNKDSAQGKLMQAYFFTQGIKSSSNPSTDEYLVKANAT
YADGYIAIKAGEPRSMDTYKLILNGKTLKGETTTEAVDAATAEKVFKQYAND
NGVDGEWTYDDATKTFTGTERSMDTYKLILNGKTLKGETTTEAVDAATAEK
VFKQYANDNGVDGEWTYDDATKTFTGTERSXXRSMDTYKLILNGKTLKGET
TTEAVDAATAEKVFKQYANDNGVDGEWTYDDATKTFTVTERSNGL

XX**: WT**
TNLCPFGEVFNATRFASVYAWNRKRISNCVADYSVLYNSASFSTFKCYGVSPT
KLNDLCFTNVYADSFVIRGDEVRQIAPGQTGKIADYNYKLPDDFTGCVIAWNS
NNLDSKVGGNYNYLYRLFRKSNLKPFERDISTEIYQAGSTPCNGVEGFNCYFP
LQSYGFQPTNGVGYQPYRVVVLSFELLHAPATVCGPK

XX**: WT(C4^{-})**
TNLCPFGEVFNATRFASVYAWNRKRISNCVADYSVLYNSASFSTFKAYGVSPT
KLNDLAFTNVYADSFVIRGDEVRQIAPGQTGKIADYNYKLPDDFTGAVIAWNS
NNLDSKVGGNYNYLYRLFRKSNLKPFERDISTEIYQAGSTPCNGVEGFNCYFP
LQSYGFQPTNGVGYQPYRVVVLSFELLHAPATVAGPK

XX**: WT(S371L)**
TNLCPFGEVFNATRFASVYAWNRKRISNCVADYSVLYNLASFSTFKCYGVSPT
KLNDLCFTNVYADSFVIRGDEVRQIAPGQTGKIADYNYKLPDDFTGCVIAWNS
NNLDSKVGGNYNYLYRLFRKSNLKPFERDISTEIYQAGSTPCNGVEGFNCYFP
LQSYGFQPTNGVGYQPYRVVVLSFELLHAPATVCGPK

XX**: WT(S373P)**
TNLCPFGEVFNATRFASVYAWNRKRISNCVADYSVLYNSAPFSTFKCYGVSPT
KLNDLCFTNVYADSFVIRGDEVRQIAPGQTGKIADYNYKLPDDFTGCVIAWNS
NNLDSKVGGNYNYLYRLFRKSNLKPFERDISTEIYQAGSTPCNGVEGFNCYFP
LQSYGFQPTNGVGYQPYRVVVLSFELLHAPATVCGPK

XX**: Omicron**
TNLCPFDEVFNATRFASVYAWNRKRISNCVADYSVLYNLAPFFTFKCYGVSPT
KLNDLCFTNVYADSFVIRGDEVRQIAPGQTGNIADYNYKLPDDFTGCVIAWNS
NKLDSKVSGNYNYLYRLFRKSNLKPFERDISTEIYQAGNKPCNGVAGFNCYFP
LRSYSFRPTYGVGHQPYRVVVLSFELLHAPATVCGPK

XX: **Omicron(4C-)**
TNLCPFDEVFNATRFASVYAWNRKRISNCVADYSVLYNLAPFFTFKAYGVSPT
KLNDLAFTNVYADSFVIRGDEVRQIAPGQTGNIADYNYKLPDDFTGAVIAWNS
NKLDSKVSGNYNYLYRLFRKSNLKPFERDISTEIYQAGNKPCNGVAGFNCYFP
LRSYSFRPTYGVGHQPYRVVVLSFELLHAPATVAGPK

XX: **Omicron(L371S)**
TNLCPFDEVFNATRFASVYAWNRKRISNCVADYSVLYNSAPFFTFKCYGVSPT
KLNDLCFTNVYADSFVIRGDEVRQIAPGQTGNIADYNYKLPDDFTGCVIAWNS
NKLDSKVSGNYNYLYRLFRKSNLKPFERDISTEIYQAGNKPCNGVAGFNCYFP
LRSYSFRPTYGVGHQPYRVVVLSFELLHAPATVCGPK

XX: **Omicron(P373S)**
TNLCPFDEVFNATRFASVYAWNRKRISNCVADYSVLYNLASFFTFKCYGVSPT
KLNDLCFTNVYADSFVIRGDEVRQIAPGQTGNIADYNYKLPDDFTGCVIAWNS
NKLDSKVSGNYNYLYRLFRKSNLKPFERDISTEIYQAGNKPCNGVAGFNCYFP
LRSYSFRPTYGVGHQPYRVVVLSFELLHAPATVCGPK

Supplementary Figures

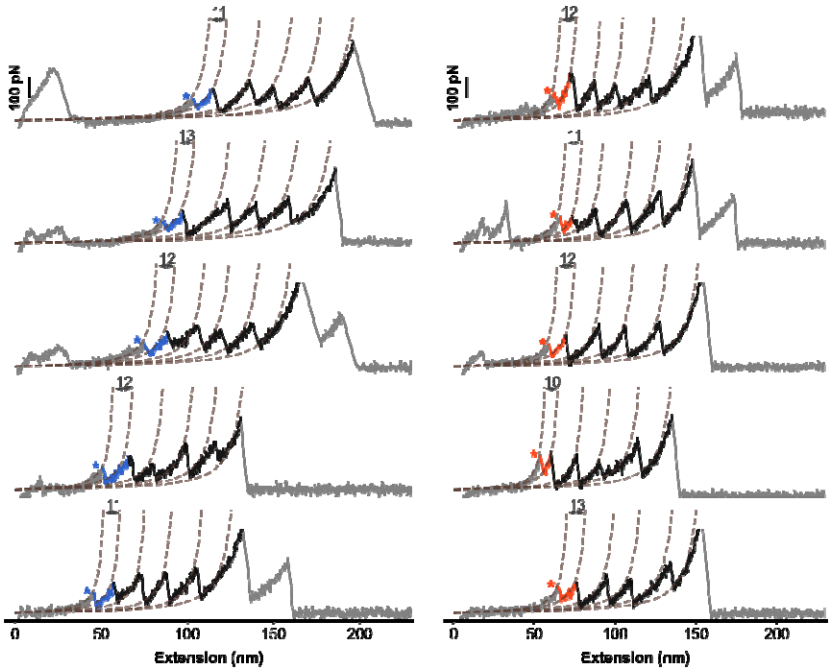

Figure S1. More representative curves of RBDs. Representative curves showing a series of sawtooth-like peaks from the unfolding of the RBD with a ΔLc of ~11 nm and marker protein GB1 with a ΔLc of ~18 nm. The Omicron and WT variants are colored orange and blue, respectively.

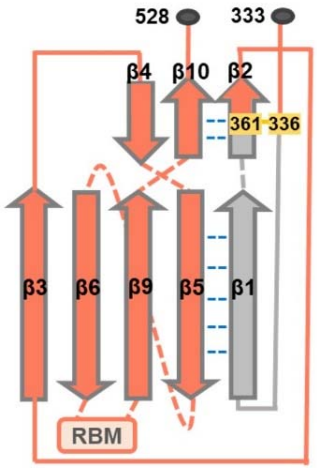

Figure S2. The unfolded fragments of RBD (4C⁻) upon unfolding. The cartoon for the unfolded secondary structures for RBD mutant with two disulfide bonds (Cys379-Cys432 and Cys391-Cys525) deleted was shown (colored in orange).

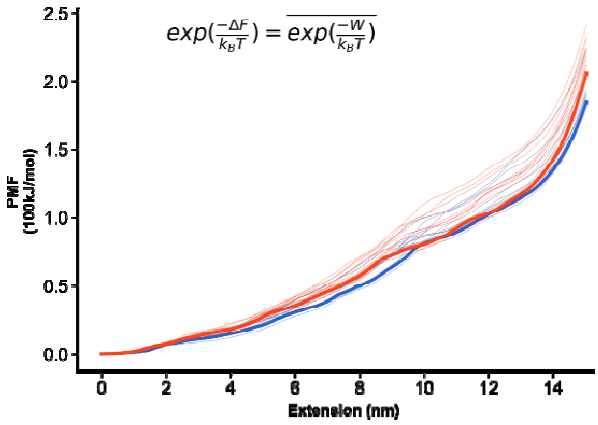

Figure S3 PMF calculation shows that Omicron is more stable than WT. PMF was calculated from irreversible pulling (v =5 Å/ns) of 10 SMD trajectories. Light color lines represent the work done in the simulations.

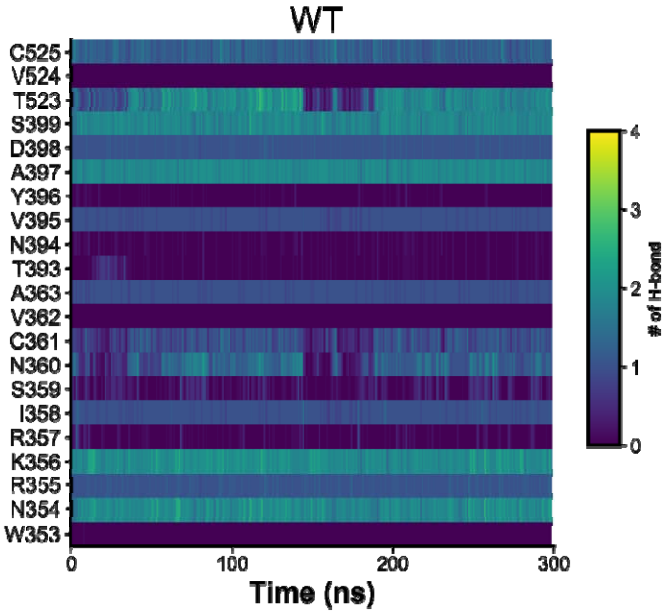

Figure S4. The evolution of H-bond number for each residue involved in β2/β10 and β1/β5 during the MD simulations for wtRBD.

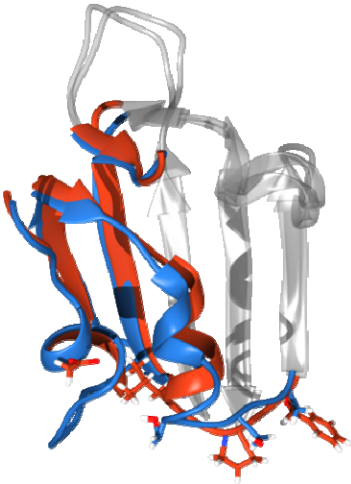

Figure S5. Overlap of the Cryo-EM structure of Omicron (red) and WT (blue). A slight conformational change closing to the β-core region of RBD is observed between Omicron and WT. The four mutations are depicted.

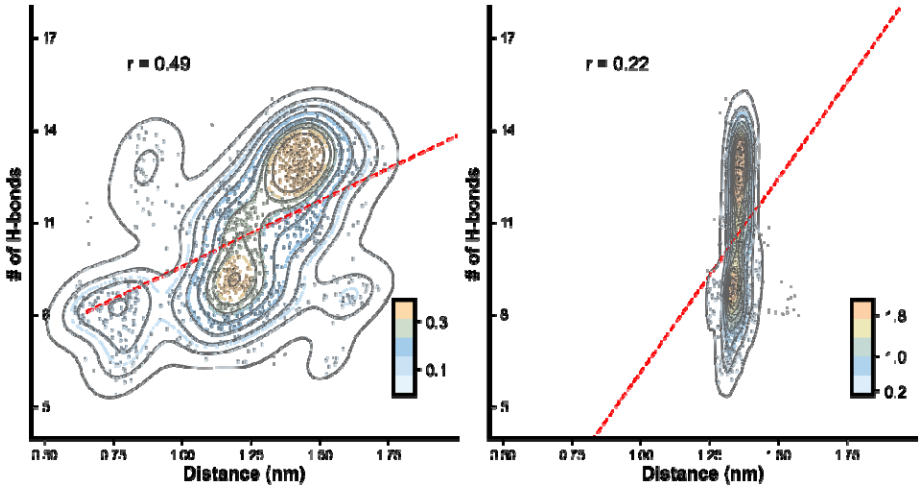

Figure S6. The relationship between the distances and the number of hydrogen bonds for different residues. The relationship between the distances of residues 371(left) / 375(right) to 432 and the number of hydrogen bonds is week.

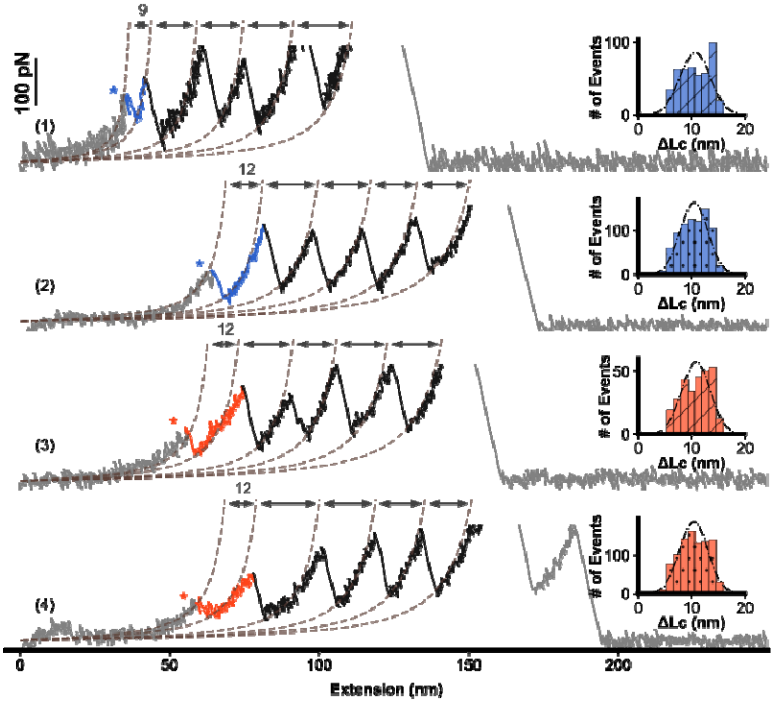

Figure S7 Representative curves of single mutation of residue 371 or 373 on RBD . Force-extension curves of RBDs of WT(S371L), WT(S373P), Omicron(L371S), and Omicron(P373S) showed the stepwise unfolding of the polyprotein, including the RBD, respectively. The histogram of ΔLc of RBD is shown in the inset.

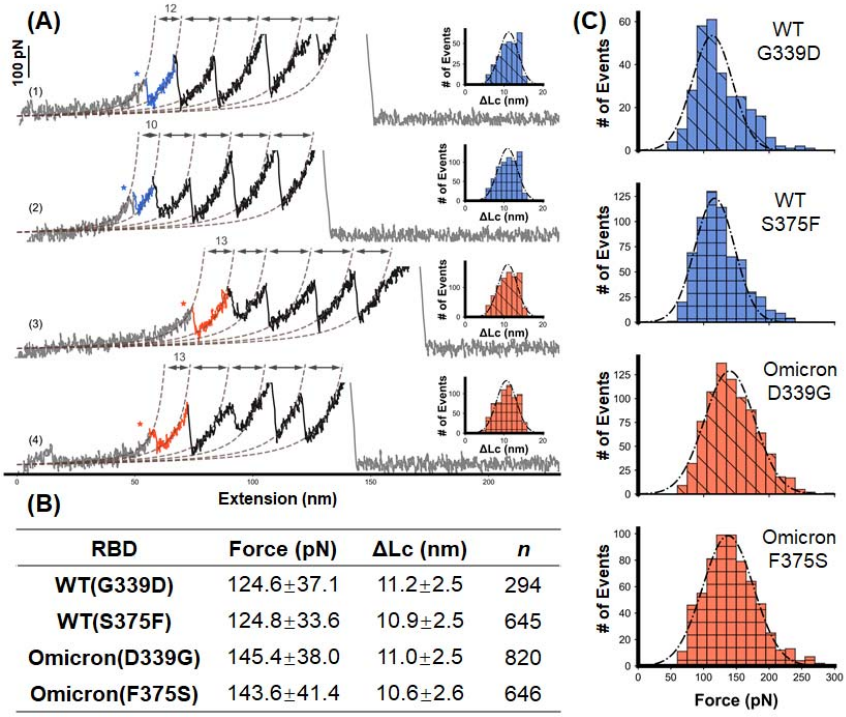

RBD	Force (pN)	ΔLc (nm)	*n*
WT(G339D)	124.6±37.1	11.2±2.5	294
WT(S375F)	124.8±33.6	10.9±2.5	645
Omicron(D339G)	145.4±38.0	11.0±2.5	820
Omicron(F375S)	143.6±41.4	10.6±2.6	646

Figure S8 AFM results of single mutation of residue 339 or 375 on RBD. A) Force-extension curves of RBDs of WT(G339D), WT(S375F), Omicron(D339G), and Omicron(F375S) showed the stepwise unfolding of the polyprotein, including the RBD, respectively. The histogram of ΔLc of RBD is shown in the inset. **B-C)** AFM unfolding results of the four mutants are shown in details.

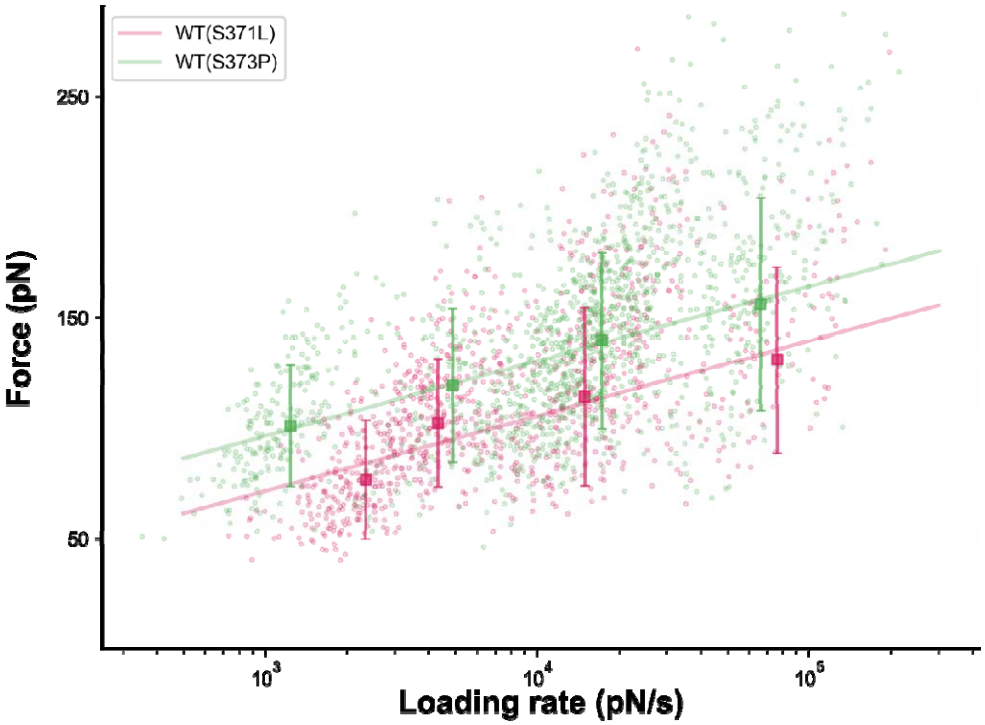

Figure S9 Dynamic force spectrum (force as a function of loading rate LR, estimated from the F vs time curves) of the unfolding of RBDs. The unfolding forces of the WT(S371L) and WT(S373P) show a linear relationship with the logarithm of the loading rate. The k_{off} was 0.53±0.79s^{-1} for the WT(S371L) and 0.10±0.04 s^{-1} for the WT(S373P). The WT(S371L) and WT(S373P) are colored pink and green, respectively.

Supplementary References:

47. R. Yang *et al.*, *J. Am. Chem. Soc.* **139**, 5351-5358 (2017).

48. W. Ott *et al.*, *Acs Nano* **11**, 6346-6354 (2017).
49. S. Shi *et al.*, *CCS Chem.* **4**, 598-604 (2022).
50. J. L. Hutter, J. Bechhoefer,. *Revi. Sci. Instrum.* **64**, 1868-1873 (1993).
51. W. Humphrey, A. Dalke, K. Schulten, *J. Mol. Graph.* **14**, 33-38, 27-38 (1996).
52. J. C. Phillips *et al.*, *J. Chem. Phys*. **153**, 044130 (2020).
53. R. B. Best *et al.*, *J. Chem. Theory Comput.* **8**, 3257-3273 (2012).
54. M. Kim, E. Kim, S. Lee, J. S. Kim, S. Lee, *J. Phys. Chem. A* **123**, 1689-1699 (2019).
55. S. Park, F. Khalili-Araghi, E. Tajkhorshid, K. Schulten, *J. Chem. Phys.* **119**, 3559-3566 (2003).
56. D. Van Der Spoel *et al.*, *J. Comput. Chem.* **26**, 1701-1718 (2005).
57. P. Virtanen *et al.*, *Nat. Methods* **17**, 261-272 (2020).

Movies S1 to S4

S1: Movie of Steering molecular dynamics (SMD) simulations of wtRBD

S2: Movie of Steering molecular dynamics (SMD) simulations of OmicronRBD

S3: Movie of MD simulations to determine the number of H-bonds of the wtRBD

S4: Movie of MD simulations to determine the number of H-bonds of the OmicronRBD